Received: 27 June 2023 | Revised: 26 July 2024 | Accepted: 1 September 2024

DOI: 10.1002/suco.202300513

ARTICLE

fib CEB-FIP WILEY

Pressure–impulse diagrams of RC beams considering fire–blast interaction

Matteo Colombo | **Paolo Martinelli**

Department of Civil and Environmental Engineering, Politecnico di Milano, Milan, Italy

Correspondence
Paolo Martinelli, Department of Civil and Environmental Engineering, Politecnico di Milano, Piazza Leonardo da Vinci 32- 20133 Milan, Italy.
Email: paolo.martinelli@polimi.it

Abstract

When analyzing military, defense, or structures/infrastructures deemed critical, explosion-induced actions—often associated with malicious actions—play a significant role. The combined effect of a blast and fire is not uncommon: in fact, an explosion can be the extreme consequence of a fire or vice versa, a fire can occur as the result of an explosion. Although advanced numerical approaches can be a proper solution for analyzing critical structures and infrastructures subjected to accidental actions, their complexity makes these approaches unsuitable for the analysis of ordinary buildings or even for the preliminary design of structures. A pressure–impulse diagram is an easy and common tool that can be adopted to verify the safety of structural members for a wide range of blast scenarios even considering the damage caused by a previous fire. This study aims to compare different approaches that can be adopted for the construction of pressure–impulse diagrams of reinforced concrete structures subjected to a blast and a blast preceded by fire. Taking as a reference case a statically indeterminate beam with three supports, this work presents the influence of the methods of analysis on the safety level assessed through pressure–impulse diagrams.

KEYWORDS

design approaches, explosion, fire, fire–blast interaction, pressure–impulse diagram, reinforced concrete structures

1 | INTRODUCTION

Fires and explosions are exceptional actions that can affect buildings and infrastructures. The causes of these accidents are various and not necessarily related to malicious acts. When analyzing military, defense, or structures/infrastructures deemed critical, such as embassies, explosion-induced actions play a significant role, even if these actions can also be critical for ordinary constructions such as residential buildings. One of the most famous blast accidents that occurred in ordinary buildings was a relatively small gas explosion on the 18th floor of the 22-story Ronan Point building that occurred in 1968, resulting in the partial collapse of the building.[1]

The combined effect of a blast and fire is not unusual: in fact, an explosion can be the extreme consequence of a fire or vice versa, a fire can occur as the result of an explosion. For example, on October 27, 2022, in Lucca (Italy), an explosion inside a two-story residential

building was followed by a fire, leading to the destruction of the building and causing two deaths and three injuries.[2] The tragic collision of two trucks on the Casalecchio junction (close to Bologna, Italy) of the A14 highway that occurred on August 6, 2018, can be regarded as an example of fire and subsequent explosion: both trucks loaded with flammable materials (GPL and chemical solvents) triggered a chain of explosions that caused the partial collapse of the overpass, causing two deaths and 145 injuries.[3]

With regard to reinforced concrete (RC) structures, in parallel with experimental campaigns involving RC structural elements such as columns, beams, plates, and walls subjected to blast loads, increasingly refined finite element (FE) numerical models have been developed. A few examples are given here.[4–8] Apart from the traditional FE method, which remains the most common choice for analyzing the structural response under blast loads, other numerical methods, such as meshfree methods and hybrid FE–meshfree methods, have been adopted to analyze RC structures subjected to blast loads. A review of the current practices in blast-resistant analysis and design of concrete structures is given in Hao et al.[9] The same study includes a good description of the numerical methods adopted in the structural response analysis under blast loading conditions. Studies (even simplified ones) on RC structures subjected to the combined action of fire and blast are much more limited.[10–16]

The refined numerical models mentioned above are not always justified for the blast-resistant analysis of ordinary buildings. For these latter structures, the use of approaches adopted in design practice is more reasonable (see, e.g., the approaches used in Stochino[17] and Krauthammer[18]). A very useful approach in the design of structural elements is the pressure–impulse (p–i) diagram, which allows the designer to verify the safety of the structure by referring to a well-defined limit state with respect to a wide range of load scenarios.[19,20] In this context, this paper discusses how the method adopted for the definition of the p–i diagram can influence the safety level of the structure by referring to a simple case of a statically indeterminate structure.

The limit state (or damage) criterion necessary for generating p–i diagrams is generally defined in terms of a displacement or deformation response. In particular, a p–i diagram provides the combination of pressure and impulse that allows the structural element to reach the considered ultimate limit state (ULS). When a specific shape of the pressure time history is considered, the pressure refers to the maximum pressure (which generally corresponds to the shock wave arrival time), while the impulse refers to the specific impulse that corresponds to the area under the pressure–time history. This diagram provides a threshold curve that divides the p–i plane into two distinct regions: the combinations of p–i that stand on the left or below the curve will not lead the structure to reach the considered ULS, while the p–i combinations that fall to the right or above the curve cannot be considered safe because they lead the structure to exceed the considered ULS. The p–i diagram method can be adopted to verify structural elements under generic blast conditions.

P–i diagrams can be generated analytically or numerically; in the latter case, a large number of pressure and impulse combinations are required to generate a reliable damage curve. Furthermore, numerical approaches can accurately describe the behavior of the p–i curve in the dynamic response domain.[9] A state-of-the-art review describing the development of the p–i diagram method over the past 70 years can be found in Chernin et al.[21] Readers can refer to the study of Abedini et al.[22] for a comprehensive overview of p–i diagrams in RC structures under blast loads.

The objective of this study is to compare various approaches for constructing p–i diagrams for RC structures exposed to blast loads, including those preceded by fire. A statically indeterminate beam with three supports is used as a reference case. This study examines how different analysis methods impact safety assessment based on p–i diagrams. It is worth noting that the analysis methods examined in this study correspond to the simplest design methods selected by the "*fib* Working Parties WP2.12.1" and outlined in the forthcoming *fib* bulletin titled "Design of Structures Subjected to Impact and Explosion."

2 | CASE STUDY

2.1 | Structure description

A one-story RC building with 2 × 2 bays on a rectangular grid of columns is considered a reference case study. Plan and elevation views are shown in Figure 1. The span lengths along the *x*- and *y*-directions are 6.6 and 5 m, respectively, while the floor-to-floor height is 3.0 m. The construction system consists of one-way beams and slabs with a uniform thickness of 0.4 m, with beams oriented along the *x*-direction and one-way slabs oriented along the *y*-direction.

The design dead load (self-weight of the slab—g_1) is set equal to 3.8 kN/m^2, while the self-weight of the beams is computed according to the beam thickness by adopting a volume unit load equal to 25 kN/m^3; the superimposed dead load (g_2) and the live load (q) acting on the prototype building are set equal to 3 and 2 kN/m^2, respectively. The accidental load combination (eq. (6.11) of EN 1990[23]) provides a load per unit length q_{acc} applied to central beam B2 equal to:

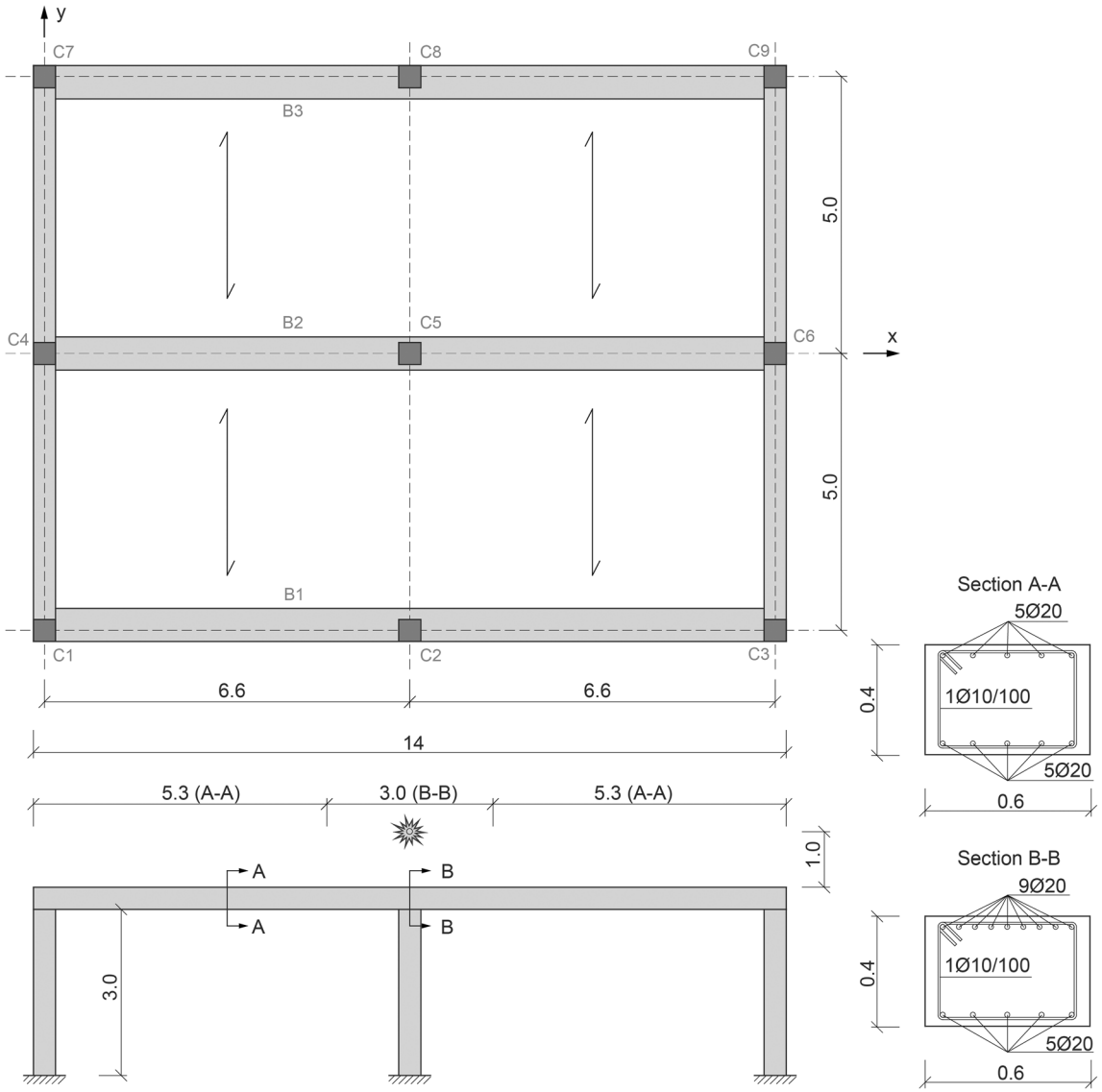

FIGURE 1 Building geometry: Plan view, front view, and beam cross-sections (measurements in meters).

$$\begin{aligned} q_{\text{acc}} &= G_k + \psi_2 \cdot Q_k \\ &= 6 + 3.8 \cdot (5 - 0.6) + 3 \cdot 5 + 0.3 \cdot (2 \cdot 5) \\ &= 40.72\,\text{kN/m} \end{aligned} \quad (1)$$

In Equation (1), the value of 6 kN/m corresponds to the beam self-weight, while the factor ψ_2 is set equal to 0.3.

A class C25/30 concrete and a type B450C high ductility rebar ($\varepsilon_{su} = 7.5\%$) are considered. Figure 1 shows the cross-sections of central beam B2. The concrete cover is assumed to be 30 mm. Central beam B2 is designed according to the Eurocode 2 standard code.[24] To avoid shear failure, a proper number of stirrups is introduced into the beams according to a traditional shear-bending moment capacity design approach. Central beam B2 is used to evaluate the potential and limitations of the design approaches presented in Section 4 in terms of p–i diagrams.

2.2 | Reference scenarios

Blast scenarios and scenarios with fire and subsequent explosion (hereafter also referred to as "fire-blast scenarios") are considered in this study. All blast and fire-blast scenarios refer to explosions with variable standoff distances and charge weights above the central column C5 (Figure 1). Two fire exposure times of 0 min (i.e., no fire) and 180 min are considered in this study. Fire-blast scenarios are characterized by fire exposure according to an ISO-834 fire curve.[25]

2.3 | Limits of applicability

This study focuses on the bending behavior of RC beams and therefore is applicable when slender structural members are considered. Moreover, this work considers blast action as a pressure distribution generated by the reflection of the shock wave over the structure, and it does not cover close-in and contact explosions. The aim of this paper is to compare different approaches for the definition of p–i diagrams and not to discuss safety verification with reference to a specific load scenario. For this reason, the present paper does not address complete—and therefore even complex—methods of analysis (such as computational fluid dynamic approaches, three-dimensional (3D) nonlinear FE analysis, etc.), but intentionally refers to simplified methods that can be easily implemented by any designer without the need for very specialized software and algorithms.

3 | SECTIONAL ANALYSIS ACCOUNTING FOR FIRE EXPOSURE

The sectional behavior of cross-sections A-A and B-B in the beam under study (Figure 1) is investigated by employing a traditional plane section approach generally used for the design of RC structural elements. This sectional analysis aims to provide a generalized constitutive law (bending moment vs. curvature relationship or M–θ) of the cross-section that is also able to account for fire exposure. An ISO-834[25] fire curve is considered, and the M–θ diagram for the cross-section is defined for the fire exposure time of interest.

The temperature distribution across the cross-section is computed through a one-dimensional finite difference heat transfer analysis of the beam over the cross-section. An ISO-834[25] fire curve is imposed at the extrados of the thickness according to Equation (2):

$$\theta = 20 + 345 \cdot \log(8t + 1). \tag{2}$$

A radiation coefficient $h = 15\ \mathrm{W/m^2K}$ and a convection constant of 0.5 are considered in the model. Nonlinear conduction is considered by adopting conductivity K_C, specific heat c_p, and density ρ as a function of temperature θ according to the formulation proposed by Eurocode 2.[26] The equations representing such parameters are given below:

$$K_C = 2 - 0.24 \cdot \left(\frac{\theta}{120}\right) + 0.012 \cdot \left(\frac{\theta}{120}\right)^2 \ [\mathrm{W/mK}], \tag{3}$$

$$\rho = \begin{cases} 2300 \left[\dfrac{\mathrm{kg}}{\mathrm{m^3}}\right], & \theta < 100^{\circ}\mathrm{C} \\ 2250 \left[\dfrac{\mathrm{kg}}{\mathrm{m^3}}\right], & \theta \geq 100^{\circ}\mathrm{C} \end{cases}, \tag{4}$$

$$c_p = 900 + 80 \cdot \left(\frac{\theta}{120}\right) - 4 \cdot \left(\frac{\theta}{120}\right)^2 \ [\mathrm{J/kgK}]. \tag{5}$$

The results of the thermal analyses are presented in Figure 2a utilizing the temperature history at different points over the cross-section depth and in Figure 2b employing the temperature distribution over the beam cross-section for an exposure time equal to 180 min.

The temperature distribution over the cross-section is instrumental in the construction of the bending moment-curvature response that is computed using a multilayer plane section approach. The compressive behavior of concrete is defined according to the constitutive law proposed by Eurocode 2[26] for fire design, whereas an elastic–perfectly plastic constitutive law is adopted for steel reinforcement.

The fire effect for each layer of the cross-section is accounted for by adopting the mechanical properties corresponding to the temperature of the layer. In particular, the evolution of mechanical properties proposed by Eurocode 2[26] for increasing temperatures is adopted here for concrete in compression and steel reinforcement. Regarding the uniaxial tensile behavior of concrete, a tension-free behavior is used. For accidental actions such as fires and explosions, the safety factors for the strengths of the materials are set to 1 according to *fib* Model Code 2010.[27]

The bending moment-curvature curves of both sagging (positive values) and hogging (negative values) bending moments are represented in Figure 3a. A simplified generalized elastic-plastic constitutive law (Figure 3b) is defined for each cross-section computing the initial cracked stiffness (EI_{cr}) as the initial slope of the M–θ curve and defining the resistant moment (M_{Rd}) and the ultimate curvature (θ_{u}) as those values that correspond to the attainment of the ultimate strain of concrete in compression ($\varepsilon_{\mathrm{cu}}$). The values of the aforementioned parameters for both cross-sections A and B and for both fire exposure times are reported in Table 1.

It is worth noting that, according to the constitutive laws provided in Eurocode 2,[26] the ultimate deformation of concrete in compression significantly increases with rising temperature, whereas the ultimate deformation of steel remains nearly constant. These factors explain the observed phenomenon in section A-A, where the compressed fibers are exposed to fire (as shown in

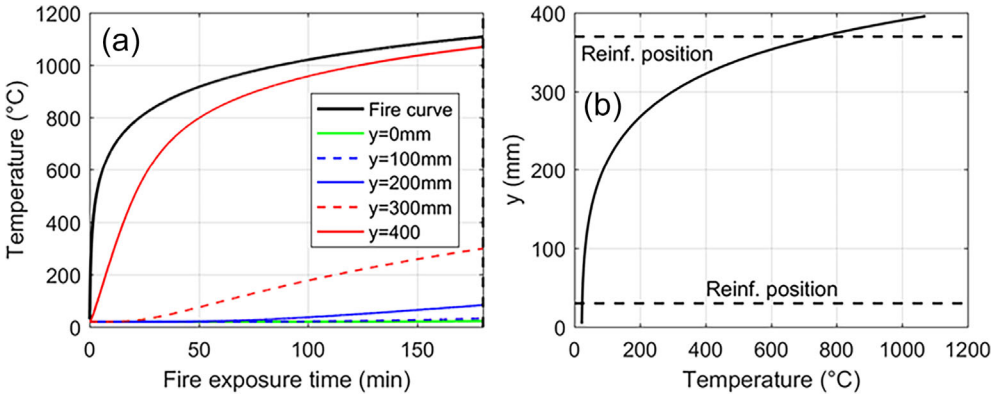

FIGURE 2 (a) Temperature–time history and (b) evolution of temperature distribution across the thickness during a 180-min fire exposure.

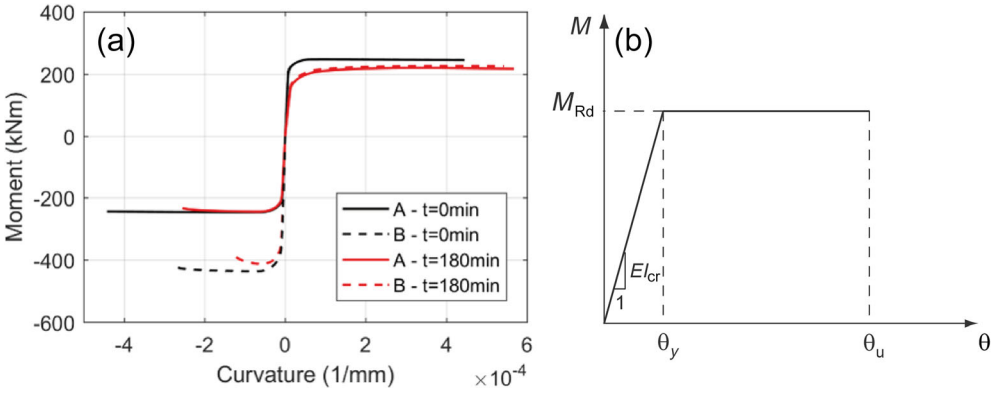

FIGURE 3 (a) Moment-curvature response at fire exposure times $t = 0$ min and $t = 180$ min (b) idealized moment-curvature response employed in numerical analyses.

TABLE 1 Flexural properties of cross-sections A-A and B-B with and without exposure to fire.

Cross-section	Fire exposure time (min)	M_{Rd} (Nm)	θ_u (1/m)	EI_{cr} (Nm^2)
A-A	0	2.43E+5	4.42E-1	2.79E+7
A-A	180	2.17E+5	5.68E-1	1.26E+7
B-B	0	4.16E+5	2.73E-1	4.28E+7
B-B	180	3.72E+5	1.33E-1	3.81E+7

Figure 1), resulting in a notable increase in the ultimate deformation of concrete and a consequent rise in ultimate curvature. In contrast, in section B-B, where the tensioned fibers are exposed to fire and subjected to a negative bending moment, the ultimate curvature decreases. This occurs because the reinforcement, primarily affected by fire, experiences minimal changes in ultimate deformation, while the compressed concrete is exposed to lower temperatures.

4 | DESIGN APPROACHES FOR THE DEFINITION OF P–I DIAGRAMS

Among the most common design approaches for the analysis of RC structures subjected to blast loads and subsequent derivation of p–i diagrams, the following are examined:

A. An analytical approach based on the "energy balance method";
B. A numerical approach based on FE analysis by using beam elements.

Approaches A and B are further subdivided as follows:

A1: analytical approach with an elastic shape function;

A2: analytical approach with a plastic shape function;

B1: linear elastic FE analysis;

B2: nonlinear FE analysis.

When a fire exposure follows a blast load, the aforementioned blast design approaches can be adopted to fix the damage level of the structure at the end of the blast phenomenon, and a traditional fire design approach can be adopted for a pre-damaged structure.

In the case where fire exposure precedes an explosion, the fire effects can be initially considered in a simplified

way by adopting temperature-dependent mechanical material properties and defining, for the cross-section, a generalized constitutive law (i.e., moment-curvature diagram) that considers fire effects and that can be used for a subsequent mechanical analysis that accounts for the blast load. This is the procedure adopted in this work.

In the case of blast loads, dynamic effects can often lead to different failure mechanisms than those expected under static conditions. All the methods under investigation define a priori the structural behavior from which the failure mechanism is derived and are unable to predict any change in the failure mechanism with increasing strain rate. A more detailed description of these methods is presented in Sections 4.1 and 4.2.

Advanced 3D nonlinear FE analyses can simulate pressure waves using computational fluid dynamics approaches. Coupled thermomechanical approaches can also be adopted to assess the damage level produced by fire before a blast load. In this last type of analysis, material properties can be defined as a function of temperature and strain rate. Three-dimensional nonlinear finite element (NLFE) analyses with solid elements can automatically consider the strain rate effect and can simulate the change in the failure mechanism due to the strain rate effect. In any case, as already stated, these methods are not covered in this paper, which simply addresses simplified tools for the design.

4.1 | Description of approach A

P–i curves generally present a vertical and a horizontal asymptote that are defined as impulsive and quasi-static asymptotes. The most common way to define such asymptotes is to use an "energy balance method" that is based on the principle of conservation of mechanical energy.[18] In particular, the definition of the impulsive asymptote is based on the assumption that, because of the inertia effects, the total energy that is initially (time equal to zero) imparted to the structure corresponds to the kinetic energy only; the impulsive asymptote can be defined by equating this energy (kinetic energy at time zero, K.E.) with the total strain energy (S.E.) stored in the system when the desired ULS is reached.

For the case of the quasi-static asymptote, the assumption that the load is constant until reaching the considered ULS allows defining this asymptote by equating the maximum possible work done by the load (W.E.) with the same total S.E. stored in the system when the desired ULS is reached (S.E.).

To represent the portion of the curve between the two asymptotes, the following formulation proposed by Baker et al.[19] for triangular load is used:

$$\text{S.E.} = \text{W.E.}\tanh^2\left(\frac{\text{K.E.}}{\text{W.E.}}\right)^{1/2}. \tag{6}$$

The "energy balance method" requires the adoption of a shape function ($\psi(x)$) to describe the displacement history ($v(x,t)$) of each point of the beam as:

$$v(x,t) = \psi(x)\cdot v_0(t), \tag{7}$$

where $v_0(t)$ is the displacement history of the selected degree of freedom. In the case under investigation, the mid-span displacement of the left-side span (equal to that of the right-side due to the symmetry of the load and geometry) is considered the reference degree of freedom of the system. The calculation of quantities W.E., K.E., and S.E. for both approaches A1 and A2 is presented in Appendix A.

4.1.1 | Approach A1

Approach A1 adopts a shape function—labeled ψ_1 and defined in Equation (8)—which corresponds to the fourth-order polynomial that respects boundary conditions and that represents a good approximation of the elastic deformation under distributed loads:

$$\psi_1(x) = 8\left(\frac{x}{l}\right)^4 - 12\left(\frac{x}{l}\right)^3 + 4\left(\frac{x}{l}\right). \tag{8}$$

Equation (8) applies to the left-side span of the beam (see Figure 1), while symmetry conditions are applied to the right-side span. In the case under investigation, the ULS corresponds to the situation in which the cross-section over the central support reaches its ultimate curvature (θ_u^-). It should be noted that for the shape function adopted, the curvature on the central support represents the maximum value on the whole beam, and for the case under consideration, the value of the ultimate curvature of cross-section B is always lower than that of cross-section A (Table 1). The energy quantities K.E., S.E., and W.E. are computed by using the simplified moment-curvature relationship discussed in Section 3, which can also account for fire exposure (Figure 3b).

4.1.2 | Approach A2

Approach A2 adopts a plastic shape function—labeled ψ_2—and is defined in Equation (9) as:

$$\psi_2(x) = 1 - \frac{\left|\left(x-\frac{l}{2}\right)\right|}{\frac{l}{2}}. \tag{9}$$

As for ψ_1 shape function, Equation (9) applies to the left-side span of the beam, while symmetry conditions are applied to the right-side span. This shape function considers two concentrated plastic hinges at the midspan and over the central support. The dimensions of these plastic hinges are considered equal to the cross-sectional characteristic length (l_{cs}), which is calculated in Equation (A12) of Appendix A adopting the proposal of the Eurocode 2 standard code[24] and taken as the crack spacing (s_r). The plastic hinge length calculated according to the Eurocode 2 standard[24] is compared with six other simplified formulations commonly used in the seismic field (Sawyer,[28] Corley,[29] Mattock,[30] Paulay and Priestley,[31] FEMA,[32] Panagiotakos and Fardis[33]). The value obtained with Eurocode 2[24] is close to the mean value of the seven formulations analyzed (results not shown here for the sake of brevity). The impulsive and quasi-static asymptote values are only marginally influenced by the plastic hinge length, and the conclusions reported in the article are not affected by the approach used to calculate the plastic hinge length.

The ULS considered is the same as approach A1 and therefore corresponds to the situation in which the cross-sections over the central support reach the ultimate curvature (θ_u^-).

4.2 | Description of approach B

Approach B consists of dynamic FE linear elastic (B1) and nonlinear (B2) analyses with beam elements. FE numerical models of central beam are built and processed by employing the software Abaqus/CAE 2021.[34] The beam is discretised with 2-node Timoshenko linear beam elements (B21) with three degrees of freedom per node (i.e., in-plane beam). A mesh size of 100 mm is considered, resulting in 136 beam elements. Horizontal and vertical movements at the column locations are prevented according to the structural scheme depicted in Figure 1.

Gravity loads are applied first through static analysis. Dynamic analyses are subsequently performed by applying the blast load as a uniform pressure distribution evolving over time. The Newmark time integration method of constant acceleration ($\beta = 0.25$, $\gamma = 0.5$) is adopted, with a time step $\Delta t = 0.001$ s. Unless otherwise specified, numerical models include the well-known Rayleigh-type viscous damping, which is proportional to the mass and initial stiffness. A damping ratio of 3.0% is imposed on the first and fourth modes.

4.2.1 | Approach B1

Approach B1 consists of linear elastic FE analyses where the internal forces/moments of the beam are computed. A traditional sectional design approach can be adopted to compare the acting maximum bending moments with the bending moment capacity computed according to a ULS design. A linear elastic material with a reduced Young's modulus and Poisson's ratio of 0.20 is adopted for the beam elements. The reduced value of Young's modulus is deduced from the values of the cracked flexural stiffness (EI_{cr}) listed in Table 1 for cross-sections A and B. The ULS considered for the derivation of the p–i diagram corresponds to the situation in which the most critical cross-section reaches its ultimate bending capacity in the sagging (M_{Rd}^+) or hogging (M_{Rd}^-) regions.

For each analysis, the value of the global safety coefficient is computed as

$$\gamma = \min\left(\left|\frac{M_{Rd}^i}{M_{Ed}^i}\right|\right), \tag{10}$$

where M_{Ed}^i and M_{Rd}^i refer to the ith cross-section (with i ranging from 1 to the number of integration points over the structure) and represent the acting bending moment computed by the analysis and the ultimate bending moment, respectively. The case of $\gamma > 1$ means that the ULS condition is not reached (safe condition), while a value of $\gamma < 1$ represents the excess of the ULS condition (failure).

4.2.2 | Approach B2

Approach B2 consists of dynamic nonlinear FE analyses where the nonlinear behavior of the material is accounted for through a simplified generalized constitutive law in terms of the bending moment-curvature, as schematically illustrated in Figure 3b. Thus, the individual FE is not assigned a law in terms of the stress and strain of materials, but is globally and directly assigned a generalized elastic-perfectly plastic (without hardening) moment-curvature law (Figure 3b). Fire exposure is accounted for by using a modified generalized constitutive law. The nonlinear behavior is thus fully described by the parameters given in Table 1, namely, the cracked flexural stiffness, ultimate resisting moment, and ultimate curvature. This approach can be described as dynamic plastic analysis using the finite element, as it combines the nonlinear cross-sectional behavior characteristic of plastic analysis with dynamic analysis conducted by an FE solver.

The ULS corresponds to the scenario where the most critical cross-section reaches its ultimate curvature (θ_u^i) in either the sagging (Sect. A-A) or hogging (Sect. B-B) region. The global safety factor is computed as follows:

$$\gamma = \min\left(\left|\frac{\theta^i_u}{\theta^i_{max}}\right|\right). \quad (11)$$

In Equation (11), θ^i_{max} represents the maximum curvatures computed during the analysis at the midspan or at the central support. A value of $\gamma > 1$ indicates that the ULS condition is not reached (safe condition), while $\gamma < 1$ indicates an excess of the ULS condition (failure).

4.2.3 | Definition of the p–i curves

The p–i curves defined by methods B1 and B2 represent the points (p–i) corresponding to a global safety coefficient γ equal to 1. Figure 4 shows the construction of the p–i curve according to method B2 for the blast scenario ($t = 0$ min). The figure represents the results of each analysis (characterized by a specific value of maximum pressure and specific impulse) in terms of safety verification. In particular, the green dots represent the load conditions for which $\gamma > 1$, while the red dots represent the load conditions that lead to exceeding the ULS ($\gamma < 1$). To define the p–i curve, a linear interpolation between the values of γ is adopted to compute all the points corresponding to the ULS threshold ($\gamma = 1$). Finally, the continuous curve is defined by the hyperbole that better interpolates these points.

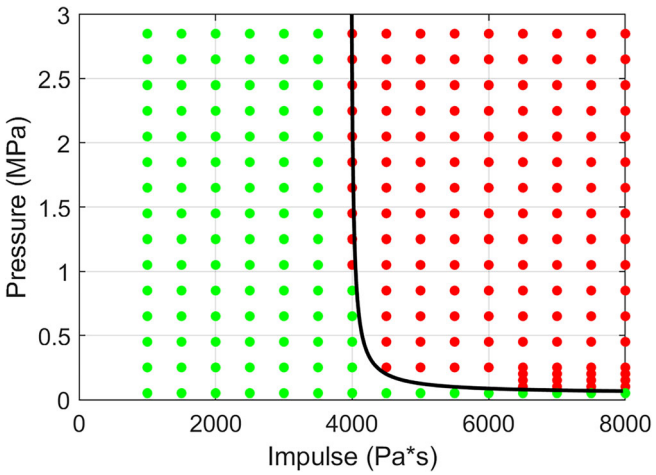

FIGURE 4 Example of the derivation of a p–i diagram.

The main characteristics of the FE numerical models B1 and B2 are summarized in Table 2. The number of analyses required for the derivation of p–i diagrams is indicated in Table 2. Since the reference is made to both blast and fire-blast scenarios, the number is multiplied by two. It is worth noting that analytical approaches based on the energy balance method do not require iterative analysis for the derivation of p–i diagrams.

5 | RESULTS AND DISCUSSION

Figure 5a shows a comparison between the vertical displacement profiles obtained with approaches A1 and B1 when the dead load is applied, while Figure 5b compares the curvature profiles for the same approaches. Both comparisons indicate that approaches A1 and B1 provide, as expected, almost identical results in the linear elastic field.

A first comparison of FE numerical models B1 and B2 for selected blast scenarios is shown in Figure 6. The role of damping is first investigated: model B1 is run both without and with damping, and the corresponding models are labeled "B1 ($\xi = 0$)" and "B1 ($\xi = 0.03$)," respectively. The results refer to the case of a peak reflected pressure of 3.16 MPa and a specific impulse of 800 Pa × s (roughly equivalent to an explosion of 10 kg of TNT placed at a distance of 1 m) in terms of the displacement time history of the midspan point for a fire exposure time $t = 0$ min and $t = 180$ min (Figure 6a, b). The maximum sagging bending moment along the beam length (M_A; Figure 6c for $t = 0$ min and Figure 6d for $t = 180$ min) and the maximum hogging bending moment on the central support (M_B; Figure 6e for $t = 0$ min and Figure 6f for $t = 180$ min) are also considered. The time histories of the bending moments are compared with the corresponding resistant bending moments represented as dashed gray lines in the graphs in Figure 6c–f.

The effect of damping is visible by comparing the bending moment time histories for the FE models with and without damping (models "B1 ($\xi = 0$)" and "B1 ($\xi = 0.03$)"). The high-frequency content in the moment responses compared to the displacement response, especially for the model without damping, can also be observed. Compared with that in the no-fire scenario

TABLE 2 Main characteristics of the FE numerical models adopted to simulate the RC beam (Mech. N.L: Mechanical nonlinearity).

Approach ID	Model ID	Type of analysis	Mech. N.L.	Number of analyses
B	B1	FEM	NO	2 × 562
B	B2	FEM	YES	2 × 507

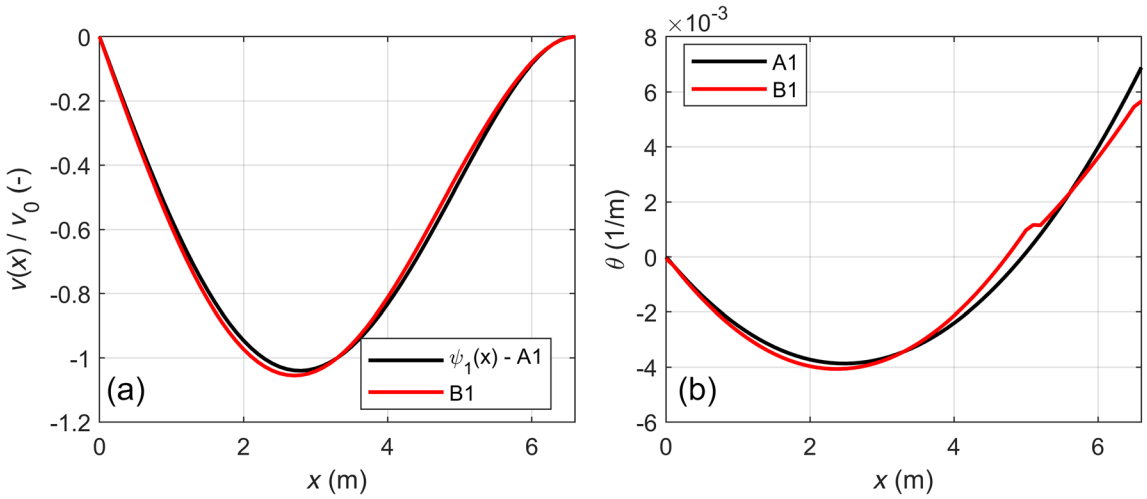

FIGURE 5 (a) Shape function ψ_1 versus deformation profile obtained from linear elastic FE analysis and (b) comparison of curvature profiles obtained from approaches A1 and B1.

($t = 0$ min), the fire damage imparted to the beam in the fire-blast scenario ($t = 180$ min) reduces the first eigenfrequency of the beam, as shown by comparing Figure 6a, b. This is a direct consequence of the fact that in the case of the fire-blast scenario, the bending stiffness of the cross-section adopted for the blast analysis is reduced by the former application of the fire curve.

The moment responses M_A and M_B of the linear elastic FE models (models B1) exceed the resistance moments M_{Rd} (dashed gray line) both at the midspan and at the central support. The application of a fire before the blast reduces the difference between the acting moments and resisting moments (Figure 6d, f) compared to the scenario without fire (Figure 6c, e).

The nonlinear analyses reach the maximum curvature at the central support (hogging moment) after approximately 0.1 s and after approximately 0.05 s for the blast and fire-blast scenarios, respectively. The attainment of the maximum curvature over the support is identified in Figure 6 with a solid circle, while the subsequent response is plotted with a lighter color. Nonlinear analyses achieve larger maximum displacements than linear analyses for blast (Figure 6a) and fire-blast scenarios (Figure 6b). In terms of moment-time histories, nonlinear analyses show smaller values—and close to the M_{Rd} values—than linear analyses due to the effect of mechanical nonlinearity (see Figure 3).

All the numerical FE models reach the corresponding ULS. In model B1, this corresponds to exceeding the resisting moment M^+_{Rd} or M^-_{Rd}, while in nonlinear model B2, it corresponds to achieving the ultimate curvature at the central support for this specific pair of pressure and impulse. Although all models indicate the attainment of an ULS for the considered scenarios, they are reached at different time instants, underlining the influence of the model used.

It is important to note that, even if the presented p–i diagrams refer to the reaching of the selected ULS, this does not necessarily mean that the structure has failed. Figure 7 illustrates the progression from the initial statically indeterminate scheme (Figure 7a) to reaching the resisting moment at the central support (Figure 7b) and finally achieving the ultimate curvature and forming a plastic hinge at the central support (Figure 7c). In nonlinear model B2, as shown in Figure 6, after reaching the maximum curvature at the central support, the corresponding cross-section cannot transfer any bending moment, resulting in the formation of a hinge (solid circle in Figure 6) over the central support. However, the structure can still resist blast action, transitioning from an initial statically indeterminate scheme (Figure 7a) to a final statically determined one (Figure 7c). In this new configuration, if a plastic hinge forms at the midspan, mechanism motion is activated, leading to failure. Alternatively, failure can occur with the formation of a first plastic hinge at the midspan with a sagging bending moment, followed by a second plastic hinge at the center support with a hogging bending moment, resulting in mechanism motion and subsequent failure. Moreover, due to the large displacement achieved in this stage, a second-order catenary action, which is not considered in the present analysis, can provide an additional contribution to resisting the blast load.

All the methods presented here do not allow a detailed measurement of the punctual strain rate because they always refer to beam kinematics. For this reason, it is complex to apply dynamic increase factors that modify the mechanical properties of materials at the punctual

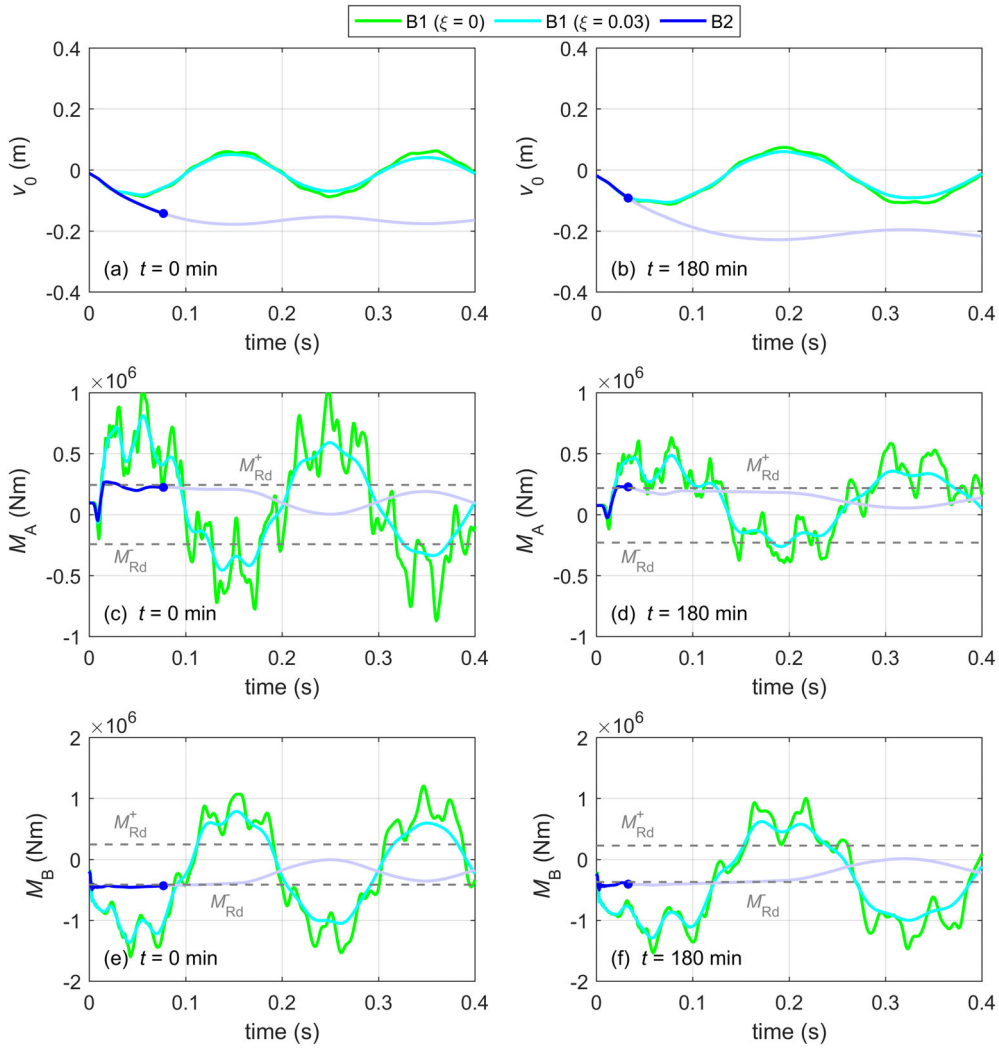

FIGURE 6 Time histories of midspan displacement (v_0) and bending moments (M_A, M_B) for numerical models B1 and B2: (a), (c), (e) blast scenario at $t = 0$ min and (b), (d), (f) fire-blast scenario at $t = 180$ min.

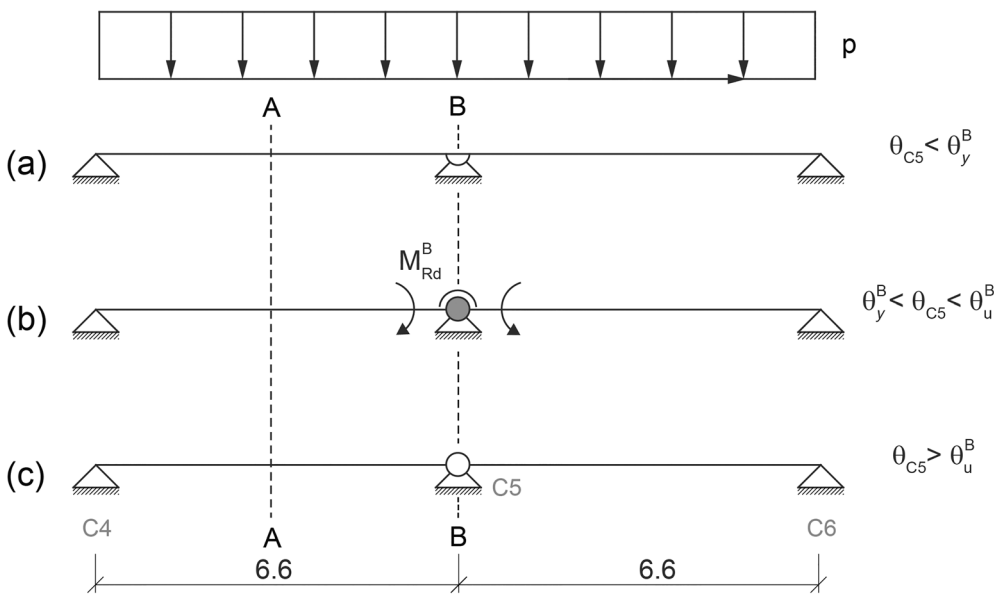

FIGURE 7 Continuous beam on three supports: (a) initial configuration, (b) achievement of resisting moment at the central support, and (c) formation of a plastic hinge at the central support.

level. Approaches similar to those proposed by the *fib* Model Code 2010[27] could be adopted, which generally propose material properties for concrete and steel reinforcement amplified by a factor that does not depend on the actual strain rate but is constant across the cross-section and throughout the analysis. The

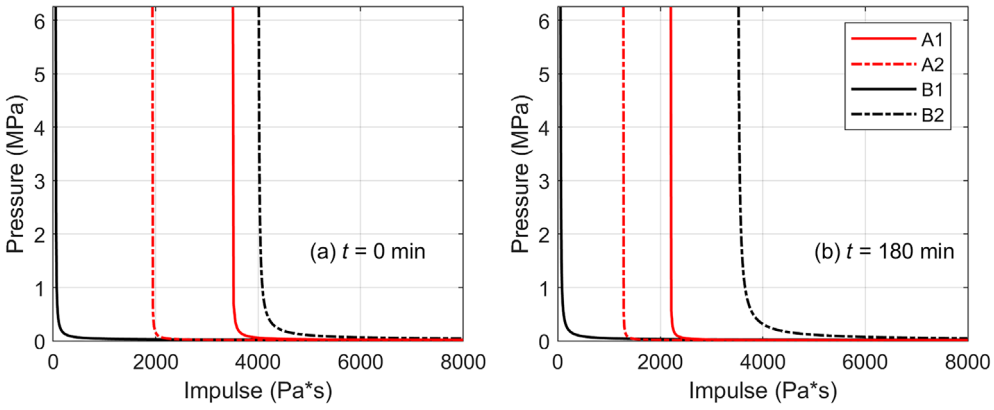

FIGURE 8 P–i diagrams for numerical approaches A1, A2, B1, and B2: (a) blast scenarios and (b) fire-blast scenarios.

TABLE 3 Asymptotes of the p–i diagrams for approaches A1, A2, B1, and B2.

	$t = 0$ min		$t = 180$ min	
Model ID	i (Pa × s)	p (MPa)	i (Pa × s)	p (MPa)
A1	3521	0.022	2212	0.017
A2	1947	0.018	1284	0.016
B1	60	0.020	55	0.018
B2	4020	0.024	3530	0.020

application of such a method would therefore be similar for all the approaches discussed and therefore would not lead to substantial differences in the relative comparison between the methodologies analyzed.

Figure 8 shows a direct comparison of all the approaches in terms of p–i diagrams for blast scenarios (Figure 8a) and fire-blast scenarios (Figure 8b). The same comparison is summarized in Table 3, where the values of impulsive (vertical) and quasi-static (horizontal) asymptotes of the p–i diagrams are reported.

First, the use of FE linear analysis (B1) leads to a very conservative beam design, especially when the structural behaviors lie in the impulsive regime (vertical asymptote). Regarding the quasi-static domain (horizontal asymptote), all approaches provide almost the same results. Approach B2 generally shows a larger safe area, thus demonstrating that the structure can significantly profit from plastic redistribution in resisting blast action. The effect of fire application is visible in a reduction in the safe area.

A further comparison between different approaches is depicted in Figure 9, where the curvature profiles are plotted for each approach under the ULS condition, close to the failure threshold in a no-fire scenario. For approaches B1 and B2, the diagrams represent analyses of the horizontal asymptote. This result shows how model B1 reaches, at the ULS considered, a very low level of deformation and is not able to profit from any ductility of the structure, thus leading to a design approach that

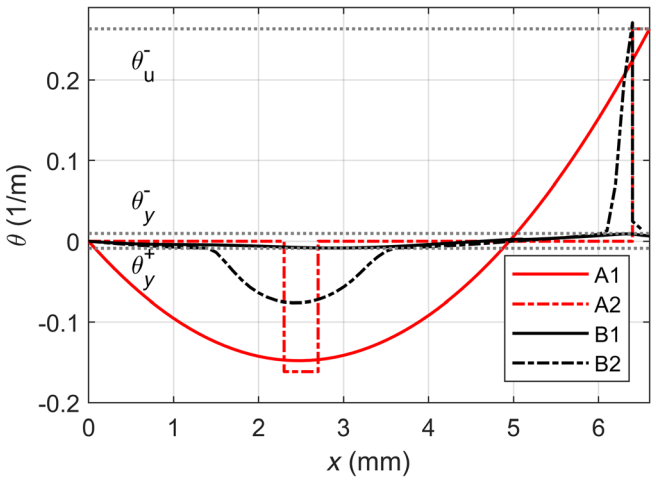

FIGURE 9 Curvature profile at the onset of ULS condition for approaches A1, A2, B1, and B2.

seems to be much too conservative, especially because of dealing with exceptional load conditions. Model A1 significantly overestimates the curvature, resulting in an unrealistic profile; this is due to the selection of the shape function and because the curvature is derived only by a kinematic approach (second derivative of the deformed shape). In contrast, model A2 concentrates all the curvatures at the plastic hinge locations (i.e., central support and midspan).

6 | CONCLUSIONS

Based on the discussed results, the following conclusions can be drawn:

- The use of different analysis approaches affects the safety evaluation of the structure. The use of mechanical nonlinear approaches in structural analysis allows consideration of structural redistribution effects that play a fundamental role in defining a more realistic resistance condition of the structure

that, especially when redundant structures are considered, can provide additional resources even when a ULS condition defined over a single cross-section is exceeded.

- P–i diagrams are a well-known tool that allows simultaneous verification of the safety of structural members for several loading scenarios. The approaches presented here consider the mechanical nonlinear behavior of the beam cross-section and define the safety for a sectional ULS condition. The method adopted for their construction plays a crucial role, thus leading to a large difference in the safety threshold. This difference can even be two orders of magnitude compared to, for instance, the impulsive asymptote in the case of elastic FE analysis (approach B1) and that of nonlinear FE analysis (approach B2).
- The use of analytical methods can provide a good design tool for simple structural members such as those considered here, but important attention should be given to the selection of the shape function.
- Analytical approaches based on the energy balance method adapt well to the design of single structural elements or simple structures; in contrast, when a more complex structure is considered, the use of NLFE approaches (even in the simplified form of linear elements with nonlinear generalized constitutive relationships) could help to avoid excessive oversizing of the structures.

ACKNOWLEDGMENT

Open access publishing facilitated by Politecnico di Milano, as part of the Wiley - CRUI-CARE agreement.

CONFLICT OF INTEREST STATEMENT

No potential conflict of interest was reported by the authors.

DATA AVAILABILITY STATEMENT

The data that support the findings of this study are available from the corresponding author upon reasonable request.

ORCID

Matteo Colombo https://orcid.org/0000-0001-6457-7894
Paolo Martinelli https://orcid.org/0000-0003-1029-7744

REFERENCES

1. Pearson C, Delatte N. Ronan point apartment tower collapse and its effect on building codes. J Perform Constr Facil. 2005;19(2):172–7. https://doi.org/10.1061/(asce)0887-3828(2005)19:2(172)
2. Esplosione a Lucca, palazzina distrutta. 2022. Accessed January 13, 2023. https://www.lanazione.it/lucca/cronaca/esplosione-a-lucca-1.8224029
3. Esplosione a Borgo Panigale: un morto, feriti, danni. Ponte crollato e A14 chiusa. 2018. Accessed January 13, 2023. https://www.bolognatoday.it/cronaca/incidente-stradale/incendio-borgo-panigale-traffico-ambulanze-vigili.html
4. Chen W, Hao H, Chen S. Numerical analysis of prestressed reinforced concrete beam subjected to blast loading. Mater Des. 2015;65:662–74. https://doi.org/10.1016/j.matdes.2014.09.033
5. Li J, Wu C, Hao H. Investigation of ultra-high performance concrete slab and normal strength concrete slab under contact explosion. Eng Struct. 2015;102:395–408. https://doi.org/10.1016/j.engstruct.2015.08.032
6. Thiagarajan G, Kadambi AV, Robert S, Johnson CF. Experimental and finite element analysis of doubly reinforced concrete slabs subjected to blast loads. Int J Impact Eng. 2015;75:162–73. https://doi.org/10.1016/j.ijimpeng.2014.07.018
7. Yuan S, Hao H, Zong Z, Li J. A study of RC bridge columns under contact explosion. Int J Impact Eng. 2017;109:378–90. https://doi.org/10.1016/j.ijimpeng.2017.07.017
8. Bermejo M, Santos A, Goicolea J, Pérez A. Evaluation of blast loads on reinforced concrete structures with finite elements. Inf la Construcción. 2015;67(539):e095. https://doi.org/10.3989/ic.13.121
9. Hao H, Hao Y, Li J, Chen W. Review of the current practices in blast-resistant analysis and design of concrete structures. Adv Struct Eng. 2016;19(8):1193–223. https://doi.org/10.1177/1369433216656430
10. Kakogiannis D, Pascualena F, Reymen B, Pyl L, Ndambi JM, Segers E, et al. Blast performance of reinforced concrete hollow core slabs in combination with fire: numerical and experimental assessment. Fire Saf J. 2013;57:69–82. https://doi.org/10.1016/j.firesaf.2012.10.027
11. Ruan Z, Chen L, Fang Q. Numerical investigation into dynamic responses of RC columns subjected for fire and blast. J Loss Prev Process Ind. 2015;34:10–21. https://doi.org/10.1016/j.jlp.2015.01.009
12. Colombo M, Martinelli P, di Prisco M. A design approach for tunnels exposed to blast and fire. Struct Concr. 2015;16(2):262–72. https://doi.org/10.1002/suco.201400052
13. Zhai C, Chen L, Xiang H, Fang Q. Experimental and numerical investigation into RC beams subjected to blast after exposure to fire. Int J Impact Eng. 2016;97:29–45. https://doi.org/10.1016/j.ijimpeng.2016.06.004
14. Pan L, Chen L, Fang Q, Zhai C, Pan T. A modified layered-section method for responses of fire-damaged reinforced concrete beams under static and blast loads. Int J Prot Struct. 2016;7(4):495–517. https://doi.org/10.1177/2041419616658384
15. Roy T, Matsagar V. Mechanics of damage in reinforced concrete member under post-blast fire scenario. Structures. 2021;31(June):740–60. https://doi.org/10.1016/j.istruc.2021.02.005
16. Colombo M, Martinelli P, Arano A, Øverli JA, Hendriks MAN, Kanstad T, et al. Experimental investigation on the structural response of RC slabs subjected to combined fire and blast. Structures. 2021;31(June):1017–30. https://doi.org/10.1016/j.istruc.2021.02.029
17. Stochino F. RC beams under blast load: reliability and sensitivity analysis. Eng Fail Anal. 2016;66:544–65. https://doi.org/10.1016/j.engfailanal.2016.05.003
18. Krauthammer T. Modern protective structures. Boca Raton: CRC Press; 2008. https://doi.org/10.1201/9781420015423

19. Baker W, Cox P, Westine P, Kulesz J, Strehlow R. Explosion hazards and evaluation. Amsterdam, The Netherlands: Elsevier Scientific; 1983.
20. Krauthammer T, Astarlioglu S, Blasko J, Soh TB, Ng PH. Pressure-impulse diagrams for the behavior assessment of structural components. Int J Impact Eng. 2008;35(8):771–83. https://doi.org/10.1016/j.ijimpeng.2007.12.004
21. Chernin L, Vilnay M, Shufrin I, Cotsovos D. Pressure-impulse diagram method—a fundamental review. Proc Inst Civ Eng Eng Comput Mech. 2019;172(2):55–69. https://doi.org/10.1680/jencm.17.00017
22. Abedini M, Mutalib AA, Raman SN, Alipour R, Akhlaghi E. Pressure–impulse (P–I) diagrams for reinforced concrete (RC) structures: a review. Arch Comput Methods Eng. 2019;26(3):733–67. https://doi.org/10.1007/s11831-018-9260-9
23. BS EN 1990. Eurocode—basis of structural design. 2005.
24. BS EN 1992-1-1. Eurocode 2: Design of Concrete Structures—part 1-1: general rules and rules for Buildings. 2004.
25. ISO 834–1. Fire resistance tests—elements of building construction Part1: general requirements. 1999.
26. EN 1992-1-2. Eurocode 2: Design of Concrete Structures—Part 1–2: general rules—structural fire design. 2004.
27. fib. Fib Model Code for Concrete Structures 2010. 2013.
28. Sawyer H. Design of concrete frames for two failure states. Proc., Int. Symp. on the flexural mechanics of reinforced concrete, ASCE-ACI. Farmington Hills: American Concrete Institute (ACI); 1965. p. 405–37. https://doi.org/10.14359/16726
29. Corley G. Rotation capacity of reinforced concrete beams. ASCE J Struct Div. 1966;92(5):121–46. https://doi.org/10.1061/JSDEAG.0001504
30. Mattock A. Discussion of rotational capacity of reinforced concrete beams by W. D. G. Corley. ASCE J Struct Div. 1967;93(2):519–22. https://doi.org/10.1061/JSDEAG.0001678
31. Paulay T, Priestley MJN. Seismic design of reinforced concrete and masonry buildings. Hoboken, NJ: John Wiley and Sons; 1992. https://doi.org/10.1002/9780470172841
32. FEMA. FEMA 356 Prestandard and commentary for the seismic rehabilitation of buildings. Federal Emergency Management Agency 2000.
33. Panagiotakos T, Fardis M. Deformations of reinforced concrete members at yielding and ultimate. ACI Struct J. 2001;98(2):135–48. https://doi.org/10.14359/10181
34. Dassault Systèmes. Abaqus Analysis User's Manual—Version 2021. 2021.

AUTHOR BIOGRAPHIES

Matteo Colombo, Department of Civil and Environmental Engineering, Politecnico di Milano, Piazza Leonardo da Vinci 32- 20133 Milan, Italy. Email: matteo.colombo@polimi.it.

Paolo Martinelli, Department of Civil and Environmental Engineering, Politecnico di Milano, Piazza Leonardo da Vinci 32- 20133 Milan, Italy. Email: paolo.martinelli@polimi.it.

How to cite this article: Colombo M, Martinelli P. Pressure–impulse diagrams of RC beams considering fire–blast interaction. Structural Concrete. 2024. https://doi.org/10.1002/suco.202300513

APPENDIX A

A.1 | PROCEDURE FOR CALCULATING W.E. AND K.E.

It is possible to define the displacement history $v(x,t)$ at each beam location (x) as follows:

$$v(x,t) = \psi_i(x) \cdot v_0(t) \tag{A1}$$

with $i = 1$, 2, respectively, for cases A1 (Equation (8)) and A2 (Equation (9)). The curvature can be defined as:

$$\theta(x,t) = \psi_i''(x) \cdot v_0(t). \tag{A2}$$

The maximum curvature $\theta_{\max}$ at a generic time instant (t) is located at $x = L$ and is equal to:

$$\theta_{\max}(t) = \psi_i''(L) \cdot v_0(t). \tag{A3}$$

The ULS condition in both cases A1 and A2 is defined by:

$$\theta_{\max} = \theta_u^{B-B} \tag{A4}$$

where θ_u^{B-B} in Equation (A4) coincides θ_u^- defined in Section 4.1. Equation (A3) allows the computation of the displacement of the equivalent single degree of freedom system at the onset of this ULS condition:

$$v_{0,u} = \frac{\theta_u^{B-B}}{\psi_i''(L)} \tag{A5}$$

The maximum possible work (W.E.) can be defined for both the approaches A1 ($i = 1$) and A2 ($i = 2$) as:

$$\text{W.E.} = \int_0^L p_R \cdot B \cdot v_u(x) \cdot dx = \int_0^L p_R \cdot B \cdot \psi_i(x) \cdot v_{0,u} \cdot dx, \tag{A6}$$

where p_R is the reflected pressure, B is the width of the competence area and $v_u(x)$ is the displacement distribution at ULS condition.

The kinetic energy at initial velocity (K.E.) is computed as follows for both approaches A1 and A2:

$$\text{K.E.} = \frac{1}{2} \cdot m \cdot \left(\frac{I}{m}\right)^2 = \frac{1}{2} \cdot \frac{i^2 \cdot B \cdot L}{\rho \cdot h}, \tag{A7}$$

where in Equation (A7) I represents the total impulse of the load time history, i is the specific impulse, m is mass of the system, L is the span of the beam, h is the thickness of the cross-section and ρ is the density of concrete.

The evaluation of the S.E. at ULS is computed differently for approaches A1 and A2.

A.2 | PROCEDURE FOR CALCULATING S.E. FOR APPROACH A1

The specific S.E. is defined by the following equations where "*sect*" refers to either A-A or B-B:

$$\begin{cases} \left(\frac{\text{S.E.}}{L}\right) = \frac{1}{2} EI_{\text{cr}}^{\text{sect}} \cdot \theta^2 & \theta \le \theta_{y,\text{sect}} \\ \left(\frac{\text{S.E.}}{L}\right) = \frac{1}{2} EI_{\text{cr}}^{\text{sect}} \cdot {\theta_{y,\text{sect}}}^2 + M_{Rd,\text{sect}}\left(\theta - \theta_{y,\text{sect}}\right) & \theta > \theta_{y,\text{sect}} \end{cases}. \tag{A8}$$

In Equation (A8), θ_y represents the curvature at yielding, while the quantities EI_{cr} and M_{Rd} were defined in Section 3.

The specific S.E. at the ULS is calculated as:

The total S.E. of the system at the ULS is:

$$\begin{cases} \left(\frac{\text{S.E.}}{L}\right)_u = \frac{1}{2} EI_{\text{cr}}^{\text{sect}} \cdot \left({\psi_1}'' \cdot v_{o,u}\right)^2 & {\psi_1}'' \cdot v_{o,u} \le \theta_{y,\text{sect}} \\ \left(\frac{\text{S.E.}}{L}\right)_u = \frac{1}{2} EI_{\text{cr}}^{\text{sect}} \cdot {\theta_{y,\text{sect}}}^2 + M_{Rd,\text{sect}}\left({\psi_1}'' \cdot v_{o,u} - \theta_{y,\text{sect}}\right) & {\psi_1}'' \cdot v_{o,u} > \theta_{y,\text{sect}} \end{cases} \tag{A9}$$

$$\text{S.E.} = \int_0^L \left(\frac{\text{S.E.}}{L}\right)_u \cdot dx. \tag{A10}$$

A.3 | PROCEDURE FOR CALCULATING S.E. FOR APPROACH A2

The S.E. is concentrated at the plastic hinge. The plastic hinge rotation at failure, φ_{u}, is defined as:

$$\varphi_{\text{u}} = \theta_u^{\text{B-B}} \cdot l_{\text{cs}}. \tag{A11}$$

In Equation (A11), l_{cs} represents the characteristic length and can be calculated according to the proposal of the Eurocode 2 standard code[24]:

$$l_{\text{cs}} = 3.4 \cdot c + 0.425 \cdot \frac{(0.8 \cdot 0.5 \cdot \emptyset)}{\rho_{s,\text{ef}}}, \tag{A12}$$

where c is the concrete cover, $\emptyset$ is the bar diameter and $\rho_{s,\text{ef}}$ is the effective reinforcement ratio. The total S.E. of the system at the ULS is given by:

$$\text{S.E.} = (2 \cdot M_{Rd,\text{A-A}} + M_{Rd,\text{B-B}}) \cdot \varphi_{\text{u}}. \tag{A13}$$